

First-principles study of stability of point defects and their effects on electronic properties of GaAs/AlGaAs superlattice

Shan Feng(冯山), Ming Jiang(姜明), Qi-Hang Qiu(邱启航), Xiang-Hua Peng(彭祥花), Hai-Yan Xiao(肖海燕), Zi-Jiang Liu(刘子江), Xiao-Tao Zu(祖小涛), and Liang Qiao(乔梁)

Citation: Chin. Phys. B, 2022, 31 (**3**): 036104. DOI: 10.1088/1674-1056/ac16cb
Journal homepage: http://cpb.iphy.ac.cn; http://iopscience.iop.org/cpb

What follows is a list of articles you may be interested in

A new direct band gap silicon allotrope *o*-Si32

Xin-Chao Yang(杨鑫超), Qun Wei(魏群), Mei-Guang Zhang(张美光), Ming-Wei Hu(胡明玮), Lin-Qian Li(李林茜), and Xuan-Min Zhu(朱轩民)

Chin. Phys. B, 2022, 31 (**2**): 026104. DOI: 10.1088/1674-1056/ac11db

First-principles study of two new boron nitride structures: C12-BN and O16-BN

Hao Wang(王皓), Yaru Yin(殷亚茹), Xiong Yang(杨雄), Yanrui Guo(郭艳蕊), Ying Zhang(张颖), Huiyu Yan(严慧羽), Ying Wang(王莹), and Ping Huai(怀平)

Chin. Phys. B, 2022, 31 (**2**): 026102. DOI: 10.1088/1674-1056/ac0a69

Prediction of scandium tetraboride from first-principles calculations: Crystal structures, phase stability, mechanical properties,and hardness

Bin-Hua Chu(初斌华) and Yuan Zhao(赵元)

Chin. Phys. B, 2021, 30 (**7**): 076107. DOI: 10.1088/1674-1056/abe116

Magnetoelectric coupling effect of polarization regulation in $BiFeO_3/LaTiO_3$ heterostructures

Chao Jin(金超), Feng-Zhu Ren(任凤竹), Wei Sun(孙伟), Jing-Yu Li(李静玉), Bing Wang(王冰), and Qin-Fen Gu(顾勤奋)

Chin. Phys. B, 2021, 30 (**7**): 076105. DOI: 10.1088/1674-1056/abf924

Ground-state structure and physical properties of YB_3 predicted from first-principles calculations

Bin-Hua Chu(初斌华), Yuan Zhao(赵元), and De-Hua Wang(王德华)

Chin. Phys. B, 2021, 30 (**4**): 046101. DOI: 10.1088/1674-1056/abcf94

First-principles study of stability of point defects and their effects on electronic properties of GaAs/AlGaAs superlattice

Shan Feng(冯山)[1,†], Ming Jiang(姜明)[1,†], Qi-Hang Qiu(邱启航)[1], Xiang-Hua Peng(彭祥花)[1], Hai-Yan Xiao(肖海燕)[1,‡], Zi-Jiang Liu(刘子江)[2], Xiao-Tao Zu(祖小涛)[1], and Liang Qiao(乔梁)[1]

[1] *School of Physics, University of Electronic Science and Technology of China, Chengdu* 610054, *China*

[2] *Department of Physics, Lanzhou City University, Lanzhou* 730070, *China*

(Received 26 April 2021; revised manuscript received 10 July 2021; accepted manuscript online 22 July 2021)

When the GaAs/AlGaAs superlattice-based devices are used under irradiation environments, point defects may be created and ultimately deteriorate their electronic and transport properties. Thus, understanding the properties of point defects like vacancies and interstitials is essential for the successful application of semiconductor materials. In the present study, first-principles calculations are carried out to explore the stability of point defects in GaAs/$Al_{0.5}Ga_{0.5}As$ superlattice and their effects on electronic properties. The results show that the interstitial defects and Frenkel pair defects are relatively difficult to form, while the antisite defects are favorably created generally. Besides, the existence of point defects generally modifies the electronic structure of GaAs/$Al_{0.5}Ga_{0.5}As$ superlattice significantly, and most of the defective SL structures possess metallic characteristics. Considering the stability of point defects and carrier mobility of defective states, we propose an effective strategy that Al_{As}, Ga_{As}, and Al_{Ga} antisite defects are introduced to improve the hole or electron mobility of GaAs/$Al_{0.5}Ga_{0.5}As$ superlattice. The obtained results will contribute to the understanding of the radiation damage effects of the GaAs/AlGaAs superlattice, and provide a guidance for designing highly stable and durable semiconductor superlattice-based electronics and optoelectronics for extreme environment applications.

Keywords: first-principles calculations, GaAs/$Al_{0.5}Ga_{0.5}As$ superlattice, point defects, electronic properties

PACS: 61.82.Fk, 61.72.uj, 73.63.–b, 61.72.Bb **DOI:** 10.1088/1674-1056/ac16cb

1. Introduction

Semiconductor superlattices (SLs), each consisting of alternating thin layers of two or more different semiconductors, exhibit unique properties and are widely used in novel optical and electronic devices.[1–4] Especially, the GaAs/AlAs SL has received wide attention in the applications of high electron mobility transistor (HEMT) and quantum cascade laser (QCL).[5–8] However, when the SL materials are used in irradiation environments such as aerospace field,[9] high energy physics field,[10] and nuclear physics field,[11] point defects may appear in GaAs/AlAs SL, resulting in the failure of the SL-based devices.[12,13] Thus, it is important to improve the performance of GaAs/AlAs SL structure under irradiation. Recently, Jiang *et al.* carried out *ab-initio* molecular dynamics (AIMD) calculations to explore its behaviors under electron irradiation and confirmed the experimental observation that the radiation resistance of GaAs/AlAs SL is enhanced by the introduction of Ga into AlAs layer.[14,15] Besides the superior radiation resistance, the GaAs/$Al_xGa_{1-x}As$ SL is also a promising candidate for electronic materials in the HEMT and QCL. Takash *et al.*[16] have fabricated a high electron mobility transistor (HEMT) with selectively doped GaAs/n-$Al_xGa_{1-x}As$ heterojunctions, and compared its mobilities and transconductance with those of GaAs MESFETs (MESFETs stand for conventional Schottky-gate field effect transistors). They found that the Hall mobility and transconductance of the HEMT at 77 K are 5.5 and 3 times higher than the corresponding values of the MESFETs, respectively, and the GaAs/n-$Al_xGa_{1-x}As$ HEMT has extremely high-speed microwave capability.[16] In the meantime, Hosako *et al.* fabricated GaAs/AlGaAs and GaSb/AlSb tetrahertz quantum aascade lasers (THz-QCL) by using a resonant longitudinal optical (LO) phonon depopulation scheme. They reported that the GaAs/AlGaAs THz-QCL has a high peak power (close to few tens of milliwatts) operation and a high operating temperature (approximate to 123 K).[17]

Thus far, a number of investigations have been carried out on GaAs/$Al_xGa_{1-x}As$ materials to explore their optical and electronic properties.[18,19] Billaha and Das have investigated the effects of Si dopant on the physical properties of GaAs/$Al_xGa_{1-x}As$-based quantum well infrared photodetector (QWIP),[20] and they found that the peak responsivity of the QWIP increases nonlinearly with the concentration of Si dopant increasing, and the peak absorption shifts toward the short wavelengths with the mole fraction of Al increasing. Goryacheva *et al.* have studied the optical transitions of GaAs/$Al_{0.45}Ga_{0.55}As$ SL at room temperature by photoreflectance spectroscopy and determined the band gap of the SL structure to be 1.5 eV.[21] Theoretically, Klos and Krawczyk

†These authors contributed equally to this work.

‡Corresponding author. E-mail: hyxiao@uestc.edu.cn

© 2022 Chinese Physical Society and IOP Publishing Ltd

calculated the band structure of GaAs/$Al_xGa_{1-x}As$ SL and estimated the ultimate efficiency of SL-based solar cells,[22] and they found that the conversion efficiency of the SL structure is higher than that of its bulk components. Besides, Billaha and Das performed the AIMD simulations to investigate the electronic spectrum of n-type GaAs/$Al_xGa_{1-x}As$ heterojunction and found that δ-doping can improve the mobility of electrons.[23]

Until now, the behaviors of GaAs/$Al_xGa_{1-x}As$ SL under irradiation environment have received relatively less attention. Expect for the studies of Jiang *et al*.,[14,15] Nobuyuki *et al*. have investigated the effects of electron irradiation on the optical and electrical properties of GaAs/$Al_xGa_{1-x}As$ heterostructures in an energy range between 5 keV and 25 keV and at electron doses of $(1\times10^{16}$–$1\times10^{21})$ electrons/cm^2,[24] and they proposed that electron irradiation induces degradation in both the optical properties and the electrical properties and observed that the most pronounced degradations happen at the energy of 10 keV. Laiadi *et al*. used the numerical simulations to compare the effect of electron irradiation with that of proton irradiation on the current–voltage characteristics of the GaAs/$Al_xGa_{1-x}As$-based solar cell,[25] and they found that the electron irradiation and the proton irradiation cause their conversion efficiencies to decrease by 5.23% and 5.60%, respectively.

Despite the studies of the optic-electronic properties and the radiation resistance of GaAs/$Al_xGa_{1-x}As$ SL reported in the literature, the stability of point defects and their effects on the electronic properties of GaAs/$Al_xGa_{1-x}As$ SL are still unknown. Motivated by these considerations, we employ density functional theory (DFT) calculations to investigate the stability of point defects in GaAs/$Al_xGa_{1-x}As$ SL and their influences on the electronic properties, including band structures, density of state distributions, in this work. In the meantime, the carrier transport properties such as effective mass and carrier mobility are determined. The results provide an insight into the radiation damage effects of the superlattice semiconductors and also contribute to improving their performance under irradiation.

2. Computational details

All the calculations are carried out by employing the density functional theory (DFT) and projector-augmented wave (PAW) method as implemented in the Vienna *ab-initio*

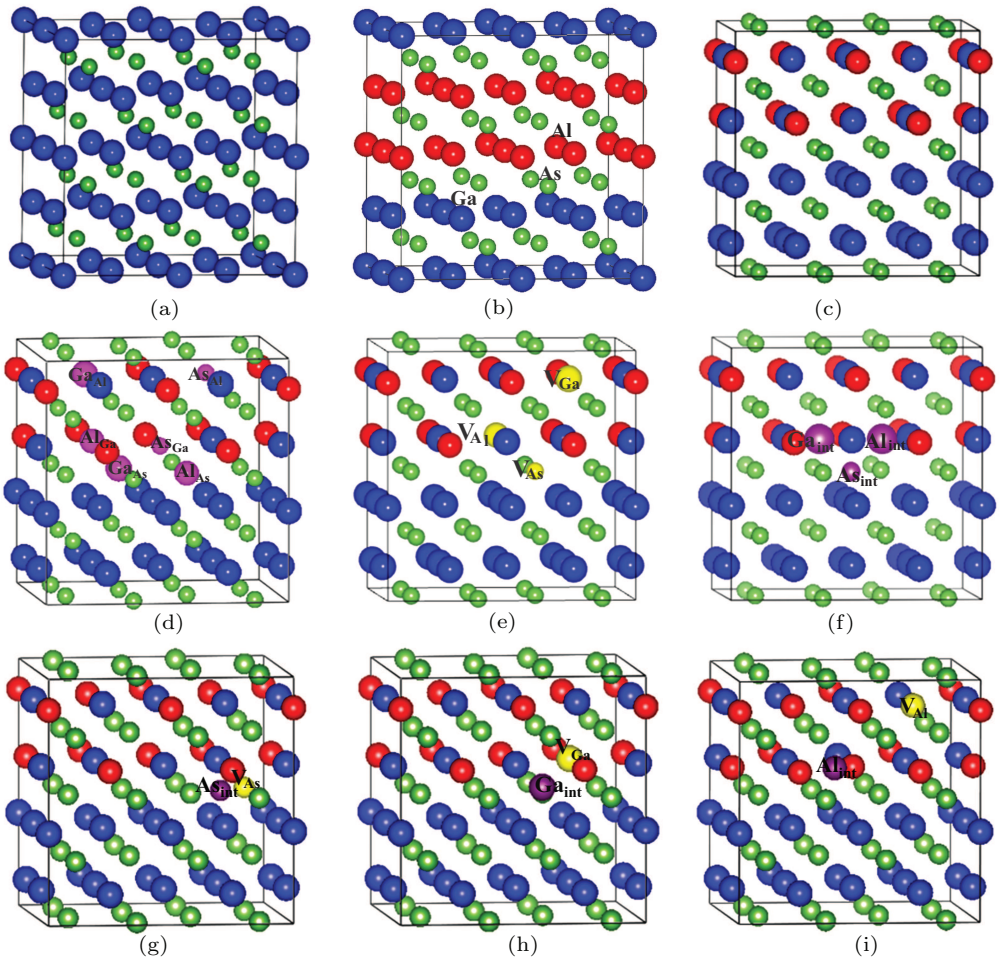


Fig. 1. Schematic view of geometrical structures of (a) bulk GaAs, (b) ideal GaAs/AlAs SL, (c) ideal GaAs/$Al_{0.5}Ga_{0.5}As$ SL, (d)–(i) defective GaAs/$Al_{0.5}Ga_{0.5}As$ SL. X_Y (X,Y = Ga, Al or As): X occupying the Y lattice site; V_X: X vacancy; X_{int}: X interstitial; X_{int}–V_X: Frenkel pairs with third neighboring X interstitial. Yellow, purple, and pink spheres represent vacancy, interstitial, and antisite sites, respectively.

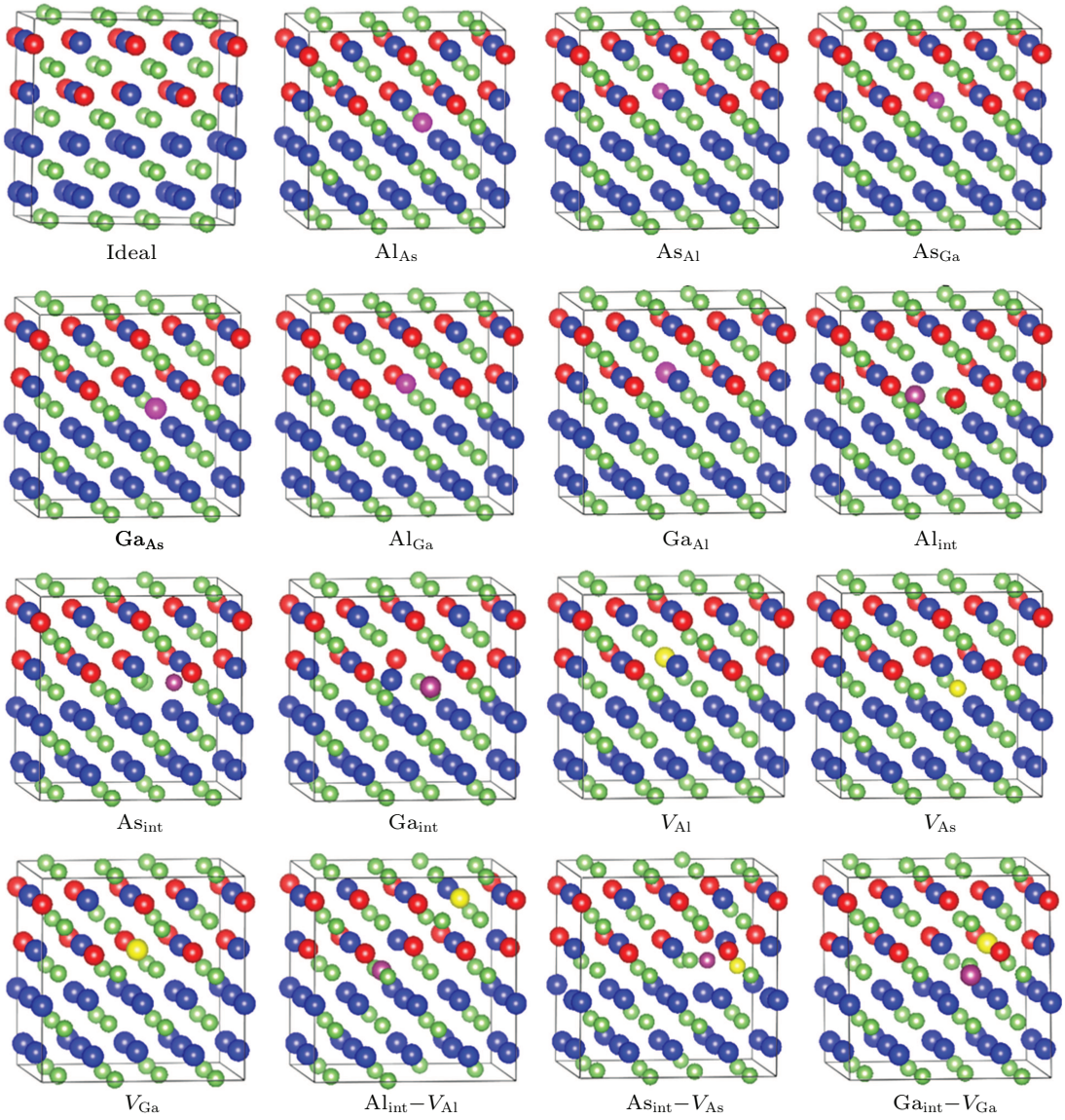


Fig. 2. Schematic view of geometrical structures of optimized ideal and defective GaAs/$Al_{0.5}Ga_{0.5}As$ SLs. X_Y (X, Y = Ga, Al or As): X occupying Y lattice site; V_X: X vacancy; X_{int}: X interstitial; X_{int}–V_X: Frenkel pairs with the third neighboring X interstitial. Yellow, purple, and pink spheres represent vacancy, interstitial, and antisite sites, respectively.

simulation package (VASP).[26,27] The generalized gradient approximation (GGA) in the Perdew–Burke–Ernzerhof (PBE)[28] functional is used to describe the exchange–correlation energy between electrons. The plane wave kinetic-energy cutoff is set as 500 eV, and Monkhorst–Pack k-point mesh is set to be $6 \times 6 \times 6$. The convergence criteria for total energy and force are 10^{-5} eV and 10^{-5} eV/Å, respectively. Previous study has demonstrated that GaAs/$Al_{0.5}Ga_{0.5}As$ SL structure may behave more robust than GaAs/AlAs SL.[14,29] In this study, the GaAs/$Al_{0.5}Ga_{0.5}As$ SL, which consists of two monolayers of GaAs alternating with two monolayers of $Al_{0.5}Ga_{0.5}As$, is considered. The structure of GaAs crystal, which is similar to that of AlAs and belongs to T_d point group of zinc blende, is shown in Fig. 1(a). Figures 1(b) and 1(c) show the geometrical structures of the ideal GaAs/AlAs SL and GaAs/$Al_{0.5}Ga_{0.5}As$ SL, respectively.

As for the defective states, the considered point defects, including antisite, interstitial and vacancy, are based mainly on our previous *ab initio* molecular dynamics simulation of the radiation damage effects of GaAs/AlGaAs superlattice,[14] in which a number of point defects are revealed and their stability are investigated. For Ga, Al, and As Frenkel pairs (FPs), the FPs with the first, second, and third-nearest neighbor interstitials have been considered. However, all FPs with the first and second-nearest neighbor interstitials are not stable, and the recombination between vacancy and interstitial occurs. Meanwhile, FPs with the third-nearest neighbor interstitials are found to be stable, which are thus selected for the subsequent calculations. Besides, this study mainly focuses on the effects of the point defects that are close to the interface of the GaAs/$Al_{0.5}Ga_{0.5}As$ superlattice on the electronic properties of the material. Schematic views of the considered point defects are illustrated in Figs. 1(d)–1(i). The geometrical structures of these defects after structural relaxation are pre-

sented in Fig. 2. It can be seen that the equilibrium geometrical structures of these defective SLs remain crystalline and there is no obvious deformation, suggesting that the introduced point defects affect the structural stability of the GaAs/$Al_{0.5}Ga_{0.5}As$ SLs slightly.

3. Results and discussion

3.1. The ground state properties of bulk GaAs, bulk $Al_{0.5}Ga_{0.5}As$, and GaAs/$Al_{0.5}Ga_{0.5}As$ SLs

The lattice constants of GaAs, $Al_{0.5}Ga_{0.5}As$, and GaAs/$Al_{0.5}Ga_{0.5}As$ SLs are determined and shown in Table 1. From the table it follows that the optimized lattice constants of GaAs and $Al_{0.5}Ga_{0.5}As$ are 5.609 Å and 5.623 Å, respectively, which agree well with the available experimental values (5.608 Å for GaAs[30] and 5.703 Å for $Al_{0.5}Ga_{0.5}As$[31]) and theoretical values (5.653 Å for GaAs.[32] and 5.648 Å for $Al_{0.5}Ga_{0.5}As$[33]). It is noted that the lattice mismatch between GaAs and $Al_{0.5}Ga_{0.5}As$ is as small as 1.443%. Thus, the medium value of 5.620 Å is used to build the structural model for GaAs/$Al_{0.5}Ga_{0.5}As$ superlattice and a $2\times2\times2$ supercell is then used. Subsequently, structural relaxation is carried out and the optimized supercell size of GaAs/$Al_{0.5}Ga_{0.5}As$ superlattice is 11.228 Å×11.228 Å×11.228 Å, which is large enough to avoid the interaction between the defect and its periodic images.

The band structures of GaAs, $Al_{0.5}Ga_{0.5}As$ and GaAs/$Al_{0.5}Ga_{0.5}As$ SL are then calculated as shown in Fig. 3. In all cases both the conduction band minima (CBM) and valence band maxima (VBM) are located at Γ points, indicative of the direct character of band gap. Furthermore, the band gap of GaAs and $Al_{0.5}Ga_{0.5}As$ are determined to be 0.52 eV and 1.13 eV, respectively, agreeing well with other theoretical results of 0.54 eV[34] and 0.86 eV,[31] respectively. The discrepancy between our results and the experimental values (1.52 eV for GaAs[32] and 2.09 eV for $Al_{0.5}Ga_{0.5}As$[35]) can be attributed to the limitation of the DFT calculations, *i.e.*, the DFT calculations generally underestimate the band gap of semiconductor materials due to the approximation of exchange–correlation functional in DFT method.[36] Besides, we find that the band gap of 1.13 eV for bulk $Al_{0.5}Ga_{0.5}As$ is larger than the value of 0.52 eV for GaAs. These results are consistent with the results of Degheidy *et al.*, who found that the band gap of $Al_{0.5}Ga_{0.5}As$ is larger than that of GaAs and smaller than that of AlAs.[37] As for GaAs/$Al_{0.5}Ga_{0.5}As$ SL, its direct band gap was calculated to be 0.84 eV. Goryacheva *et al.* have measured the band gap of GaAs/$Al_{0.45}Ga_{0.55}As$ SL to be 1.50 eV,[21] which is larger than our result.

Table 1. Calculated values of lattice constant (a) and band gap (E_g) of bulk GaAs and $Al_{0.5}Ga_{0.5}As$ and available experimental and theoretical results.

	GaAs		$Al_{0.5}Ga_{0.5}As$	
	a (Å)	E_g (eV)	a (Å)	E_g (eV)
Our Cal.	5.609	0.52	5.623	1.13
Other Cal.	5.608[a]	0.54[c]	5.703[e]	0.86[e]
Exp.	5.653[b]	1.52[b]	5.648[f]	2.09[h]

[a]Ref. [30]; [b]Ref. [32]; [c]Ref. [34]; [e]Ref. [31]; [f]Ref. [33]; [h]Ref. [35].

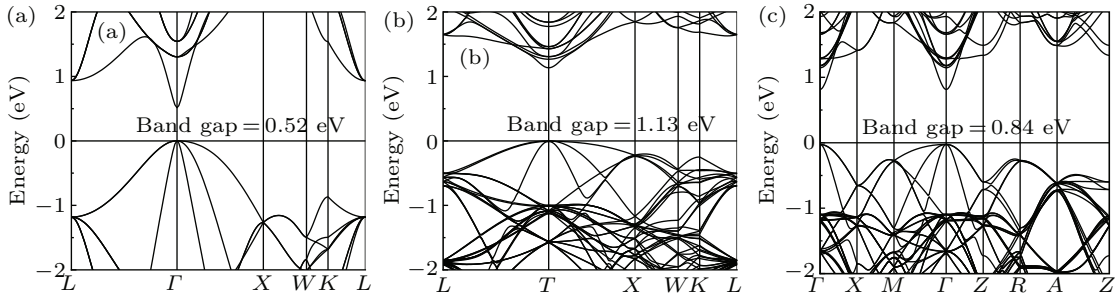


Fig. 3. Band structures of (a) bulk GaAs, (b) bulk $Al_{0.5}Ga_{0.5}As$, and (c) GaAs/$Al_{0.5}Ga_{0.5}As$ SL. The Fermi level is set to be 0 eV.

3.2. Formation energy of point defects in GaAs/$Ga_{0.5}Al_{0.5}As$ SL

The defect formation energy can be calculated from $E_f = E_{def} - E_{undef} + \sum_i \Delta n_i \mu_i$ where E_{def} is the total energy of the defective GaAs/$Ga_{0.5}Al_{0.5}As$ SL after relaxation, E_{undef} is the total energy of the ideal SL, Δn_i is the change in the number of species i (i = Ga, Al or As), and μ_i is the chemical potential of species i.[37] The E_f of GaAs/$Al_{0.5}Ga_{0.5}As$ SL is then calculated under As-rich condition, *i.e.*, $\mu_{As} = \mu_{As}^{bulk}$, $\mu_{Al} = \mu_{AlAs}^{bulk} - \mu_{As}^{bulk}$, and $\mu_{Ga} = \mu_{GaAs}^{bulk} - \mu_{As}^{bulk}$ and under cation-rich condition, *i.e.*, $\mu_{Al} = \mu_{Al}^{bulk}$, $\mu_{Ga} = \mu_{Ga}^{bulk}$, and $\mu_{As} = (\mu_{SL}^{bulk} - N_{Al}\mu_{Al}^{bulk} - N_{Ga}\mu_{Ga}^{bulk})/N_{As}$, where N_{Al}, N_{Ga}, and N_{As} represent the numbers of Al, Ga, and As atoms, respectively. In this study, the chemical environment for defect formation energy calculations is taken into consideration out of two reasons. First, the change in stoichiometry may exist during material synthesis.[38–40] For example, Gorai *et al.* have synthesized the flower-like dendritic Cu_2S crystals from $Cu(NO_3)_2$ and thiourea via solvothermal route, and they found that the stoichiometry of copper sulphide depends on reaction time at a constant temperature.[41] Second, the change in stoichiometry can also be a result of radiation damage. In the

literature, it has been reported that the irradiation can lead the stoichiometric ratio of elements in the surface layer and films to change.[42–44] Hence, "cation-rich condition" and "anion-rich condition" are considered in calculating the formation energy of different defects in this work.

As shown in Table 2, the As_{Al} (As occupying the Al lattice site) and the Al_{Ga} (Al occupying the Ga lattice site) antisite defects have negative formation energy values of 0.03 eV and 0.46 eV under As-rich condition, respectively, indicating that their formation are exothermic process. For As_{Ga} (As occupying the Ga lattice site) and Ga_{Al} (Ga occupying the Al lattice site) antisite defects, their formation energy values are determined to be 0.07 eV and 0.47 eV, respectively. Our calculations suggest that these antisite defects form easily in GaAs/$Al_{0.5}Ga_{0.5}$As SL under As-rich condition. Under cation-rich condition, the Al_{As} (Al occupying the As lattice site), Ga_{As} (Ga occupying the As lattice site), Al_{Ga} and Ga_{Al} are more favorable than As_{Ga} and As_{Al} antisite defects as indicated by their relatively small formation energy values of 0.14, 1.02, −0.55, and 0.56 eV, respectively.

Table 2. Defect formation energy (in unit eV) of GaAs/$Al_{0.5}Ga_{0.5}$As SL under As-rich and cation-rich conditions. X_Y (X, Y = Ga, Al or As): X occupying Y lattice site; V_X: X vacancy; X_{int}: X interstitial; X_{int}–V_X: Frenkel pairs with the third neighboring X interstitial as shown in Figs. 1(g)–1(i).

Defect type		As-rich	Cation-rich
Antisite	Al_{As}	5.02	1.02
	Ga_{As}	4.21	0.14
	As_{Ga}	0.07	4.14
	As_{Al}	–0.03	4.09
	Al_{Ga}	–0.46	–0.55
	Ga_{Al}	0.47	0.56
Vacancy	V_{As}	4.09	2.06
	V_{Al}	1.94	4.03
	V_{Ga}	2.00	4.04
Interstitial	As_{int}	2.59	4.62
	Al_{int}	5.15	3.07
	Ga_{int}	4.32	2.29
Frenkel pair	Al_{int}–V_{Al}	4.69	
	As_{int}–V_{As}	5.36	
	Ga_{int}–V_{Ga}	4.41	

In the case of vacancy defects, the V_{Al} (Al vacancy) and V_{Ga} (Ga vacancy) defects show similar stabilities as indicated by their similar formation energy values under both As-rich and cation-rich conditions. It is noted that the V_{Al} and V_{Ga} are more energetically favorable than V_{As} under As-rich condition, while the V_{As} is more preferable than V_{Al} and V_{Ga} under cation-rich condition. Besides, it is noted that the formation energy values for interstitial and FP defects are generally high as shown in Table 2. The preferable interstitial defects are found to be As and Ga interstitial under As- and Ga-rich conditions, respectively, and the respective formation energy values are 2.59 eV and 2.29 eV. For the FPs, it is found that they are difficult to form due to their relatively high formation energy values.

The defect formation energy values in GaAs/$Al_{0.5}Ga_{0.5}$As SL structure are plotted in Fig. 4. One can see from Fig. 4 that the Al_{Ga} antisite is the most favorable defect in GaAs/$Al_{0.5}Ga_{0.5}$As SL. Besides, except for the Al_{Ga} antisite, other antisite defects like As_{Ga}, As_{Al}, Ga_{Al}, and Ga_{As} are also favorable. Jiang *et al.* employed an AIMD method to explore the radiation resistance of GaAs/$Al_{0.5}Ga_{0.5}$As SL.[14] Their studies showed that the antisite defects are generally easier to form under electron irradiation, which is consistent with our results. Figure 4 also shows that in most cases the stability of point defects depends on the chemical environment of chemical species. A similar phenomenon has been observed in other materials. In the literature, Xiao *et al.* found that the stable chemical potential region for pure $Cs_2AgBiBr_6$ is narrow, and the Br-poor/Bi-rich condition is preferred for suppressing the formation of the Bi vacancy and Ag–Bi antisite defects, which is beneficial for maximizing the photovoltaic performance.[45] Baierle *et al.* performed spin-polarized DFT calculations of the electronic and structural properties of vacancies and antisites in zigzag, armchair, and chiral SiC nanotubes, and reported that the formation energy for antisite defects in SiC nanotubes can be affected by the chemical potential of Si and C.[46] Shu *et al.* investigated the stability of various surface point defects in p-type-doped GaAs nanowires by the first-principles calculations. Their results suggested that As antisite (As_{Ga}) is a highly stable surface point defect under As-rich condition, and reducing As chemical potential (or As partial pressure) is a feasible method to suppress the influence of AsGa defects on the p-type-doped GaAs nanowires.[47]

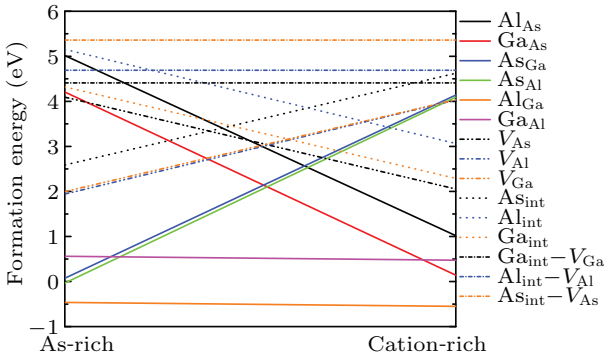


Fig. 4. Defect formation energy values of GaAs/$Al_{0.5}Ga_{0.5}$As SLs under As-rich and cation-rich conditions. X_Y (X, Y = Ga, Al or As): X occupying the Y lattice site; V_X: X vacancy; X_{int}: X interstitial. X_{int}–V_X: Frenkel pairs with the third neighboring X interstitial as shown in Figs. 1(g)–1(i).

3.3. Effects of point defects on electronic properties of GaAs/$Al_{0.5}Ga_{0.5}$As SL

Considering the preferability of antisite defects in GaAs/$Al_{0.5}Ga_{0.5}$As SL, we explore their effects on the band structures of GaAs/$Al_{0.5}Ga_{0.5}$As SL first. Figure 5 shows the band structures of GaAs/$Al_{0.5}Ga_{0.5}$As SL with different types

of antisite defects. For the Al_{As} and Ga_{As} antisite defective states, their corresponding band structures are similar to each other, which may be due to the fact that the Al and Ga chemical elements have similar valence electronic configurations, *i.e.*, $3s^2 3p^1$ for Al and $4s^2 4p^1$ for Ga. Comparing with the valence electronic configurations of As atom ($4s^2 4p^3$), we find that the formation of Al_{As} and Ga_{As} antisite defects is accompanied by introduction of extra holes, *i.e.*, p-type doping. As shown in Figs. 5(a) and 5(d), the impurity levels cross the Fermi level and lead to the metallic character of the defective SL structures. When the As_{Al} and As_{Ga} antisite defects are created in GaAs/$Al_{0.5}Ga_{0.5}$As SL, more electrons are introduced. On the other hand, the Fermi levels shift from 3.14 eV for ideal SL to 3.77 eV and 3.86 eV for As_{Al} and As_{Ga} antisite defective states, respectively. These results suggest that the As_{Al} and As_{Ga} antisite defects act as donors in the GaAs/$Al_{0.5}Ga_{0.5}$As SL, indicative of n-type doping. Figures 5(b) and 5(c) show that the impurity levels are delocalized in the forbidden band, which may influence the carrier transport properties of GaAs/$Al_{0.5}Ga_{0.5}$As SL significantly.[48] The band structures for Ga_{Al} and Al_{Ga} antisite defects are shown in Figs. 5(e) and 5(f), respectively.

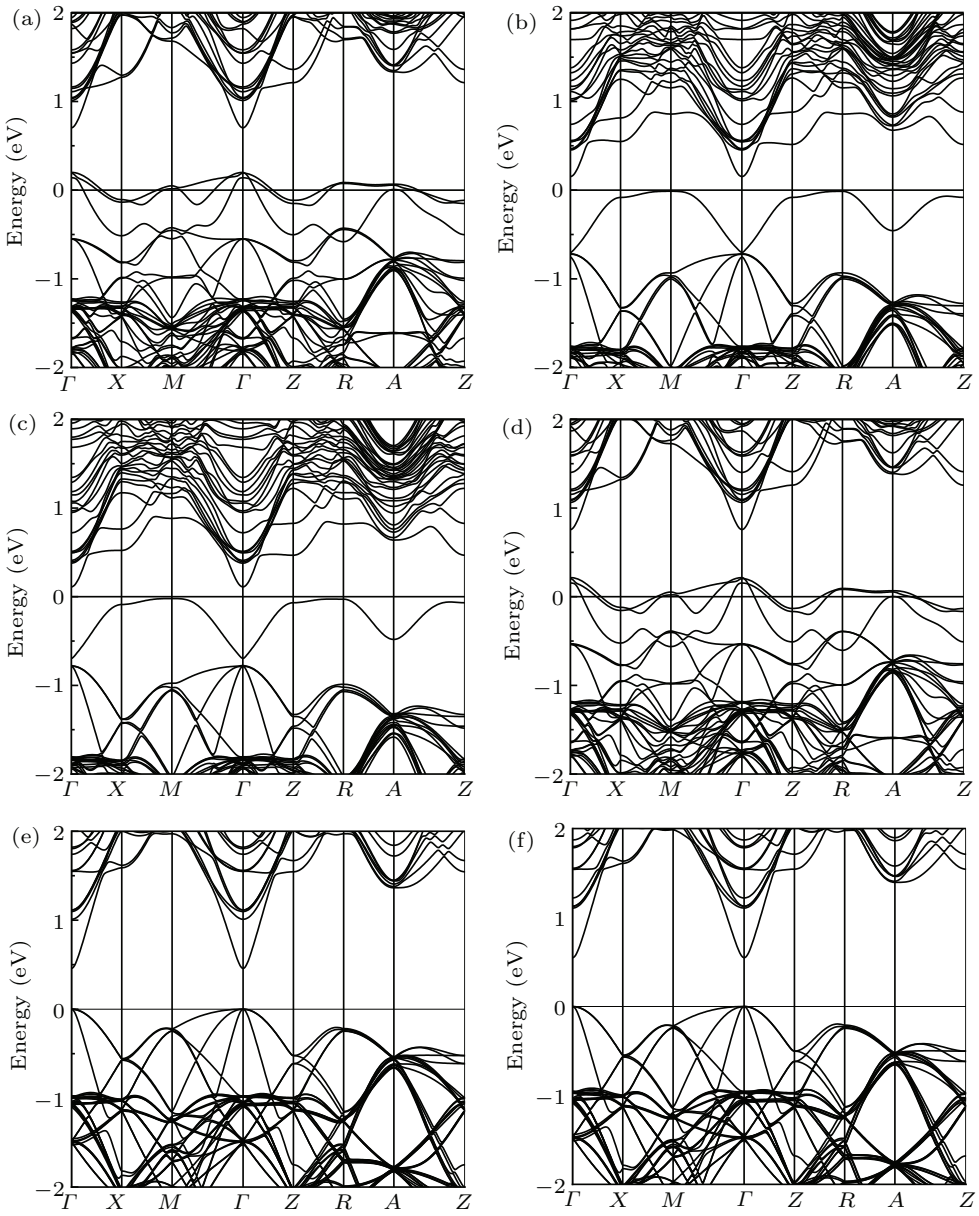


Fig. 5. Band structures of GaAs/$Al_{0.5}Ga_{0.5}$As SL with (a) Al_{As}, (b) As_{Al}, (c) As_{Ga}, (d) Ga_{As}, (e) Ga_{Al} and (f) Al_{Ga} antisite defect. X_Y (X,Y = Ga, Al or As): X occupying the Y lattice site, The Fermi level is set to be 0 eV.

Owing to the similar valence electronic configurations of Al and Ga chemical elements, the Al_{Ga} and Ga_{Al} antisite defects show similar characters in band structures. Besides, they have slight effects on the shape of band structure and reduce only the band gap of GaAs/$Al_{0.5}Ga_{0.5}$As SL from 0.84 eV to 0.55 eV and 0.46 eV, respectively. It is noted that the defective SLs with Ga_{As} and Al_{As} antisite defects show metallicity, while the defective SLs with $As_{Al}As_{Ga}$, Al_{Ga}, and Ga_{Al} an-

tisite defects still have the characters of semiconductor with the band gaps of 0.11 eV, 0.15 eV, 0.55 eV, and 0.46 eV, respectively. In order to further understand the effects of antisite defects on the electronic structure of GaAs/$Al_{0.5}Ga_{0.5}As$ SL, the partial density of state (PDOS) distribution of the defective SL is plotted in Fig. 6. As shown in Fig. 6(a), the CBM of ideal GaAs/$Al_{0.5}Ga_{0.5}As$ SL is mainly contributed by Ga-4s and Ga-4p orbitals, and the VBM is mainly contributed by As-4p orbitals. When the Al_{As} and Ga_{As} antisite defects are introduced into the SL structure, the impurity levels cross the Fermi level, resulting in metallic character of the SL as shown in Figs. 6(b) and 6(e). Besides, the impurity levels are found to be mainly contributed by the hybridization between As-4p orbitals and Ga-4p orbitals. As for the As_{Al} and As_{Ga} antisite defective states (see Figs. 6(c) and 6(d)), their band gaps decrease obviously, as compared with the value of ideal state. This is mainly due to the fact that the introduced point defects produce the impurity levels that are close to the VBM in the forbidden band. Meanwhile, the band gaps of Al_{Ga} and Ga_{Al} defective states (see Figs. 6(f) and 6(g)) decrease slightly, because the CBM shifts toward low energy level while the VBM remains nearly intact.

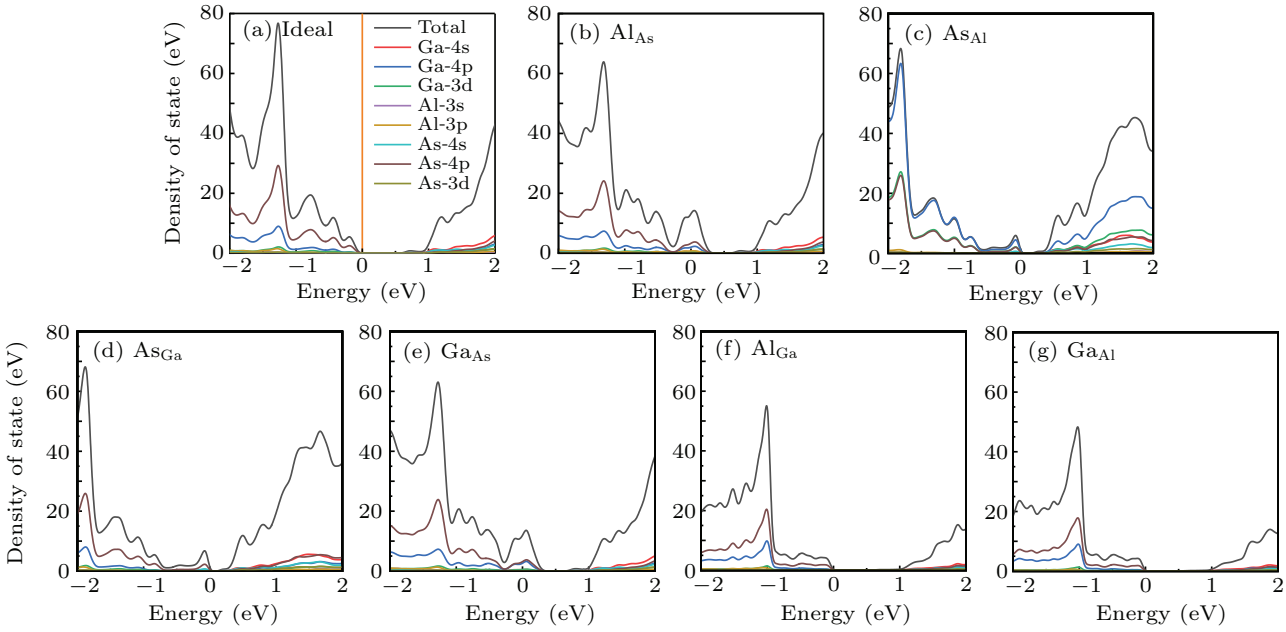


Fig. 6. Partial density of state for (a) ideal and (b)–(g) defective GaAs/$Al_{0.5}Ga_{0.5}As$ SL. X_Y (X,Y = Ga, Al or As): X occupying the Y lattice site. The Fermi level is set to be 0 eV.

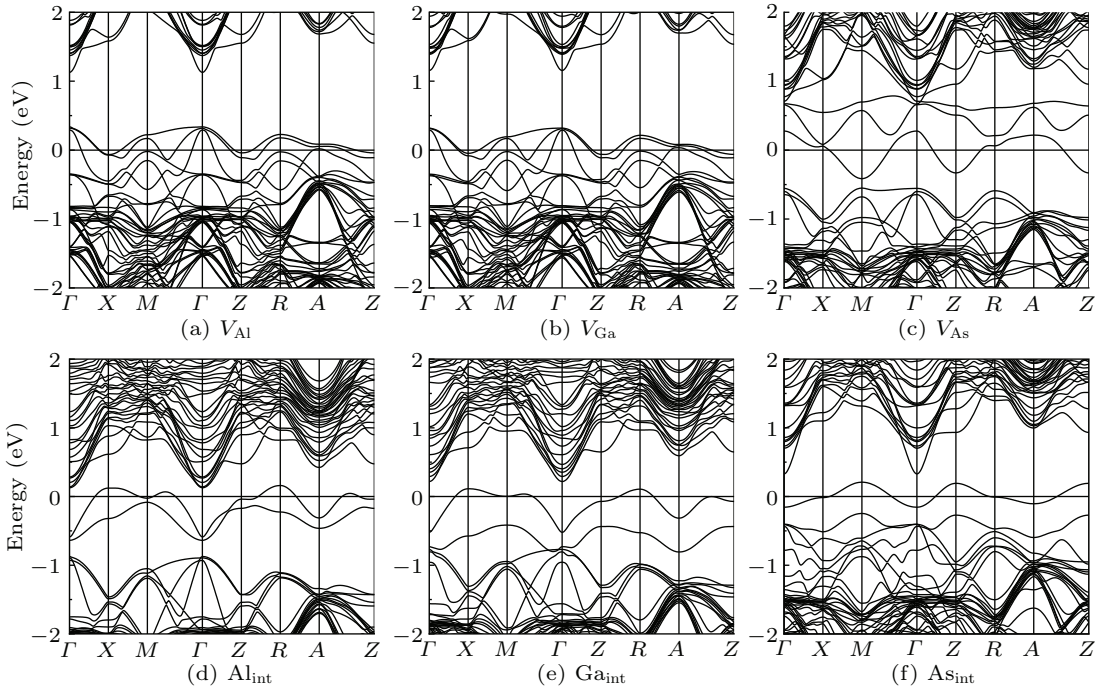


Fig. 7. Band structures of GaAs/$Al_{0.5}Ga_{0.5}As$ SL with (a) As_{int}, (b) Al_{int}, (c) Ga_{int}, (d) V_{As}, (e) V_{Al}, and (f) V_{Ga} defect. V_X (X = Al, Ga or As): X vacancy; X_{int}: X interstitial. The Fermi level is set to be 0 eV.

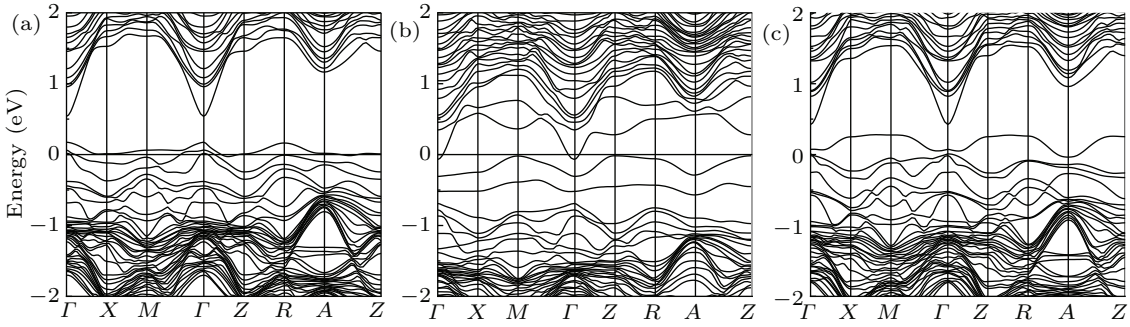


Fig. 8. Band structures of GaAs/$Al_{0.5}Ga_{0.5}As$ SL with (a) Ga_{int}–V_{Ga}, (b) As_{int}–V_{As}, (c) Al_{int}–V_{Al} Frenkel pair defects. X_{int}–V_X: Frenkel pairs with the third neighboring X interstitial as shown in Figs. 1(g)–1(i). The Fermi level is set to be 0 eV.

The band structures of GaAs/$Al_{0.5}Ga_{0.5}As$ SL with vacancy and interstitial defects are plotted in Fig. 7. The V_{Al} and V_{Ga} defects can be regarded as p-type dopants, and the impurity levels cross the fermi level and affect the valence bands considerably as shown in Figs. 7(a) and 7(b). In contrast, the V_{As} defect shown in Fig. 7(c) acts as an n-type dopant and the conduction bands are influenced considerably, for which the Fermi level is also crossed. We find that the nearest atoms around the vacancy defects are equally displaced toward the empty lattice site, which results in the charges transferring between atoms more easily, *i.e.*, the shallow impurity levels caused by point defects will result in high concentration of the carriers in the SLs.[48] For the interstitial defects, the Al_{int} and Ga_{int} defects act as n-type dopants, while the As_{int} defect is regarded as a p-type dopant. As shown in Figs. 7(d)–7(f), the impurity levels cross the Fermi level in all cases, indicating that the SLs with interstitial defects are metallic. The band structures of GaAs/$Al_{0.5}Ga_{0.5}As$ SL with Ga, As, and Al FPs (see Figs. 1(g)–1(i)) are presented in Figs. 8(a)–8(c). In all cases, the impurity levels cross the Fermi level and lead to metallic characters.

There is no doubt that the introduced point defects modify the electronic structure of GaAs/$Al_{0.5}Ga_{0.5}As$ SL significantly, and the defective SL structure generally is of metallic character, except for the As_{Al}, As_{Ga}, Al_{Ga}, and Ga_{Al} defective states. In the meantime, although the As_{Al}, As_{Ga}, Al_{Ga}, and Ga_{Al} defective SLs still remain semiconducting, their band gaps decrease significantly.

3.4. Effects of point defects on transport properties of GaAs/$Ga_{0.5}Al_{0.5}As$ SL

The electron mobility at 0 K can be calculated from the equation $\mu = e\tau/m^*$,[49] where e is the electron charge, τ is the relaxation time, and m^* is the effective mass of carrier. The electron effective masses can be determined from the equation[49–51]

$$\frac{1}{m^*} = \frac{1}{\hbar^2}\frac{\partial^2 E(k)}{\partial k^2}.$$

Here, $\hbar$ is the reduced Planck constant, k is the wave vector, and $E(k)$ is the energy of CBM. According to Fig. 3(a), the electron effective mass of bulk GaAs is calculated to be $0.056m_e$, which agrees well with the experimental value of $0.057m_e$.[52] The relaxation time of 0.48 ps for bulk GaAs reported by Gonzalez *et al.*[53] is employed in this study. The electron mobility of bulk GaAs at 0 K is determined to be 1.501×10^4 cm^2/V·s, which is higher than the experimental value of 0.942×10^4 cm^2/V·s.[54] We also calculate the electron mobility of GaAs/$Al_{0.5}Ga_{0.5}As$ SL to be 1.380×10^4 cm^2/V·s, which is larger than the value of 1.0×10^4 cm^2/V·s for GaAs/AlAs SL.[55] The results demonstrate that the GaAs/$Al_{0.5}Ga_{0.5}As$ SL may have better performance than GaAs/AlAs SL in applications like HEMT, for which high carrier mobility is needed. Meanwhile, the hole mobility of GaAs/$Al_{0.5}Ga_{0.5}As$ SL is also considered to make a comparison with that of p-type-doped defects, which is calculated to be 0.065×10^4 cm^2/V·s.

The corresponding electron or hole effective mass and carrier mobility for ideal and defective GaAs/$Al_{0.5}Ga_{0.5}As$ SLs along the Γ–X direction have been summarized in Table 3. For the antisite defects, the Al_{As} and Ga_{As} defects act as acceptors while the As_{Ga} and As_{Al} defects can function as donors in the defective GaAs/$Al_{0.5}Ga_{0.5}As$ SLs. Comparing with the ideal state, the calculated electron effective mass for As_{Ga} and As_{Al} increase, and the electron mobility of GaAs/$Al_{0.5}Ga_{0.5}As$ SL decreases from 1.38×10^4 cm^2/V·s to 1.154×10^4 cm^2/V·s and 1.214×10^4 cm^2/V·s, respectively. For the p-type-doped Al_{As} and Ga_{As} defects, they have positive effects on the hole mobility, since the calculated hole mobility of 0.122×10^4 cm^2/V·s for Al_{As} defect and 1.21×10^4 cm^2/V·s for Ga_{As} defect are larger than the value of 0.065×10^4 cm^2/V·s for ideal state. In the case of Al_{Ga} antisite defects, the electron mobility is improved while the hole mobility decreases, but in the case of Ga_{Al}antisite defects, the electron mobility and hole mobility both decrease. As for the interstitial, vacancy and FP defects, the electron mobility of GaAs/$Al_{0.5}Ga_{0.5}As$ SL decreases significantly due to the existence of these types of defects. On the other hand, the hole mobility of GaAs/$Al_{0.5}Ga_{0.5}As$ SL also decreases except As_{int} and V_{Al} defects, for which the hole mobilities are 0.153×10^4 cm^2/V·s and 0.114×10^4 cm^2/V·s, respectively.

Our calculations show that the effects of point defects on the transport properties of GaAs/$Al_{0.5}Ga_{0.5}As$ SL are generally negative, while the Al_{Ga} antisite defect enhances the electron mobility remarkably and the Al_{As}, Ga_{As}, As_{int}, and V_{Al} defects increase the hole mobility significantly. Considering the relatively high formation energy of As_{int} and V_{Al} defects, we thus propose that introduction of Al_{As}, Ga_{As}, and Al_{Ga} antisite defects into GaAs/$Al_{0.5}Ga_{0.5}As$ SLs may be an effective strategy to improve the carrier mobilities of the SL-based devices. Since this study focuses mainly on the influences of interfacial point defects and the considered defects are all located in the vicinity of the interface of the GaAs/$Al_{0.5}Ga_{0.5}As$ superlattice, the conclusion drawn in this work may be applicable to other $(GaAs)_m/(Al_{0.5}Ga_{0.5}As)_n$ $(m+n>2)$ superlattices.

Table 3. Calculated values of band gap (E_g), electron (positive value) or hole (negative value) effective mass (m^*), and electron or hole mobility (μ) along Γ–X direction in Brillouin zone for GaAs/$Al_{0.5}Ga_{0.5}As$ SL. X_Y (X,Y = Ga, Al or As): X occupying the Y lattice site; V_X: X vacancy; X_{int}: X interstitial; X_{int}–V_X: Frenkel pairs with the third neighboring X interstitial as shown in Figs. 1(g)–1(i).

Defect type		E_g (eV)	m^* (m_e)		μ (10^4 cm^2/V·s)	
			Electron	Hole	Electron	Hole
Ideal		0.84	0.051	–1.075	1.380	0.065
Antisite	Al_{As}	–		–0.575		0.122
	Ga_{As}	–		–0.577		0.121
	As_{Ga}	0.11	0.061		1.154	
	As_{Al}	0.15	0.058		1.214	
	Al_{Ga}	0.55	0.033	–3.685	2.130	0.019
	Ga_{Al}	0.46	0.118	–1.852	0.601	0.038
Interstitial	As_{int}	–		–0.460		0.153
	Al_{int}	–	0.163		0.466	
	Ga_{int}	–	0.115		0.612	
Vacancy	V_{As}	–	–		–	
	V_{Al}	–		–0.617		0.114
	V_{Ga}	–		–2.304		0.031
Frenkel	Al_{int}–V_{Al}	–	0.279	–1.401	0.252	0.050
	As_{int}–V_{As}	–	1.374	–4.032	0.051	0.017
	Ga_{int}–V_{Ga}	–	0.273	–8.772	0.258	0.008

4. Conclusions

In summary, the stabilities of point defects in $Ga_{0.5}Al_{0.5}As$/GaAs superlattice and their effects on the electronic structure and transport properties of superlattice structure have been investigated by density functional theory calculations. The results show that the antisite defects are generally dominant under As-rich and cation-rich conditions, and the interstitial and FPs defects are much more difficult to form. The band structures of the GaAs/$Al_{0.5}Ga_{0.5}As$ superlattice are modified significantly by most of the point defects, and the defective SLs are generally of metallic character except the As_{Ga}, As_{Al}, Al_{Ga}, and Ga_{Al} defective states. The further calculations show that the electron or hole mobility of GaAs/$Al_{0.5}Ga_{0.5}As$ superlattice is generally reduced due to the existence of point defects, while the Al_{As}, Ga_{As}, and Al_{Ga} antisite defects, which can form easily in $Ga_{0.5}Al_{0.5}As$/GaAs superlattice, can improve the hole or electron mobility of the SL considerably. The results suggest that intentional introduction of Al_{As}, Ga_{As}, and Al_{Ga} antisite defects can improve the carrier transport properties of GaAs/$Al_{0.5}Ga_{0.5}As$ superlattice.

Acknowledgements

The theoretical calculations were performed using the supercomputer resources at TianHe-1 in the National Supercomputer Center in Tianjin.

Project supported by the NSAF Joint Foundation of China (Grant No. U1930120), the Key Natural Science Foundation of Gansu Province, China (Grant No. 20JR5RA211), and the National Natural Science Foundation of China (Grant No. 11774044).

References

[1] Hamdi A H, Tandon J L, Vreeland T and Nicolet M A 2011 *MRS Online Proceeding Library Archive* **37** 319
[2] Barkissy D, Nafidi A, Boutramine A, Charifi H, Elanique A and Massaq M 2016 *J. Low Temp. Phys.* **182** 185
[3] Zheng Z, Zu X T, Zhang Y and Zhou W 2020 *Mater. Today Phys.* **15** 100262
[4] Zhang S, Wang J F, Wen S Z, Jiang M, Xiao H Y, Ding X, Wang N, Li M L, Zu X T, Li S A, Yam C Y, Huang B and Qiao L 2021 *Phys. Rev. Lett.* **126** 176401
[5] Tseng W, Pellegrino J, Kim J, Thurber R, Comas J, Papanicolou N and Prokes S 1992 *J. Electrochem. Soc.* **139** 1219
[6] Schrottke L, Lu X, Rozas G, Biermann K and Grahn H T 2016 *Appl. Phys. Lett.* **108** 102102
[7] Irber D M, Seidl J, Carrad D J, Becker J, Jeon N, Loitsch B, Winnerl J, Matich S, Doblinger M, Tang Y, Morkotter S, Abstreiter G, Finley J J, Grayson M, Lauhon LJ and Koblmuller G 2017 *Nano Lett.* **17** 4886
[8] Cui J G, Zhang X, Yan X, Li J S, Huang Y Q and Ren M X 2014 *Acta Phys. Sin.* **63** 136103 (in Chinese)
[9] Plis E A, Gautam N, Kutty M N, Myers S, Klein B, Schuler-Sandy T, Naydenkov M and Krishna S 2011 *Nanophotonics and Macrophotonics for Space Environments V* **8164** 893706
[10] Lin T T, Wang L, Wang K, Grange T and Hirayama H 2018 *Appl. Phys. Express* **11** 112702

[11] Perreault C S, Vohra Y K, dos Santos A M and Molaison J J 2020 *J. Magn. Magn. Mater.* **507** 5
[12] Feng S S, Lv S S, Chen L and Li Z C 2021 *Chin. Phys. B* **30** 056105
[13] Dong L F, Yang Y J, Fan W L, Han Y, Shuai W and Hong X J 2010 *Acta Phys. Sin.* **59** 1367 (in Chinese)
[14] Jiang M, Xiao H Y, Peng S M, Yang G X, Gong H F, Liu Z J, Qiao L and Zu X T 2019 *J. Nucl. Mater.* **516** 228
[15] Jiang M, Xiao H Y, Peng S M, Qiao L, Yang G X, Liu Z J and Zu X T 2018 *Nanoscale Res. Lett.* **13** 301
[16] Takash, Mimura, Satoshi, Hiyamizu, Toshio, Fujii, Kazuo and Nanbu 1980 *Jpn. J. Appl. Phys.* **19** 5
[17] Hosako I, Sekine N, Yasuda H and Hirakawa K 2006 *2006 Joint 31st International Conference on Infrared Millimeter Waves and 14th International Conference on Teraherz Electronics* p. 564
[18] Ren L and Chang B K 2011 *Chin. Phys. B* **20** 087308
[19] Peter A J and Lakshminarayana V 2008 *Chin. Phys. Lett.* **25** 3021
[20] Billaha A and Das M K 2016 *Opto-Electron. Rev.* **24** 25
[21] Goryacheva V D, Mironova M S and Komkov O S 2018 *International Conference Physica Spb* **1038** 012124
[22] Klos J W and Krawczyk M 2009 *J. Appl. Phys.* **106** 510
[23] Billaha A and Das M K 2016 *Opto-Electron. Rev.* **24** 25
[24] Nobuyuki, Tanaka, Tomonori and Ishikawa 1994 *J. Electron. Mater.* **23** 341
[25] Laiadi W, Meftah A and Sengouga N 2013 *Superlattices and Microstructures* **58** 44
[26] Kresse G and Furthmuller J 1996 *Phys. Rev. B* **54** 11169
[27] Qiao L, Zhang S, Xiao H Y, Singh D J, Zhang L K H, Liu Z J, Zu X T and Li S 2018 *J. Mater. Chem. C* **6** 1239
[28] Posselt M, Gao F, Weber W J and Belko V 2004 *J. Phys.: Condens. Matter* **16** 1307
[29] Jenčič I, Bench M W, Robertson I M and Kirk M A 1991 *J. Appl. Phys.* **69** 128
[30] Ahmed R, Hashemifar S J, Akbarzadeh H, Ahmed M and Fazal E A 2007 *Comput. Mater. Sci.* **39** 580
[31] Mao Y, Liang X X, Zhao G J and Song T L 2014 *J. Phys.: Conf. Ser.* **490** 012172
[32] Campo V L and Cococcioni M 2010 *J. Phys.: Condens. Matter* **22** 055602
[33] Vegard L Z 1921 *Zeitschrift für Physik A Hadrons and Nuclei* **5** 17
[34] Ribeiro M, Fonseca L R C and Ferreira L G 2011 *Europhys. Lett.* **94** 27001
[35] Varshni Y P 1967 *Physica* **34** 149
[36] Payne M C, Teter M P, Allan D C, Arias T A and Joannopoulos J D 1992 *Rev. Mod. Phys.* **64** 1045
[37] Degheidy A R and Elkenany E B 2012 *Mater. Sci. Semicond. Process.* **15** 505
[38] Ghigna P, Barbi G B, Chiodelli G, Spinolo G, Malavasi L and Flor G 2000 *J. Solid State Chem.* **153** 231
[39] Tsevas K, Smith J A, Kumar V, Rodenburg C, Fakis M, Yusoff A B, Vasilopoulou M, Lidzey D G, Nazeeruddin M K and Dunbar A D F 2021 *Chem. Mater.* **33** 554
[40] Kilroy W P, Ferrando W A and Dallek S 2001 *J. Power Sources* **97-8** 336
[41] Gorai S, Ganguli D and Chaudhuri S 2005 *Mater. Lett.* **59** 826
[42] Zdorovets M V, Kurlov A S and Kozlovskiy A L 2020 *Surf. Coatings Technol.* **386** 125499
[43] Tripathi N, Rath S, Kulriya P K, Khan S A, Kabiraj D and Avasthi D K 2010 *Nucl. Instrum. Methods Phys. Res. Sect. B* **268** 3335
[44] Ieshkin A E, Kireev D S, Tatarintsev A A, Chernysh V S, Senatulin B R and Skryleva E A 2020 *Surf. Sci.* **700** 121637
[45] Xiao Z W, Meng W W, Wang J B and Yan Y F 2016 *Chemsuschem* **9** 2628
[46] Baierle R J, Piquini P, Neves L P and Miwa R H 2006 *Phys. Rev. B* **74** 155425
[47] Shu H B, Yang X D, Liang P, Cao D and Chen X S 2016 *J. Phys. Chem. C* **120** 22088
[48] Cheng J P, Wang Y J, McCombe B D and Schaff W 1993 *Phys. Rev. Lett.* **70** 489
[49] Nazir S, Kahaly M U and Schwingenschloegl U 2012 *Appl. Phys. Lett.* **100** 201607
[50] Feng S, Wang N, Li M L, Xiao H Y, Liu Z J, Zu X T and Qiao L 2021 *J. Alloys Compd.* **861** 157984
[51] Tan, M R, Liu Q H, Sui N, Kang Z H, Zhang L Q, Zhang H Z, Wang W Q, Zhou Q and Wang Y H 2019 *Chin. Phys. B* **28** 056106
[52] Włodzimierz and Nakwask 1995 *Physica B* **210** 1
[53] Gonzalez B, Palankovski V, Kosina H, Hernandez A and Selberherr S 1999 *Solid-State Electron.* **43** 1791
[54] Stillman G E, Wolfe C M and Dimmock J O 1970 *J. Phys. Chem. Solids* **31** 1199
[55] Kusters R M, Wittekamp F A, Singleton J, Perenboom J, Jones G A C, Ritchie D A, Frost J E F and Andre J P 1992 *Phys. Rev. B* **46** 10207